



AFRL-RX-WP-TP-2009-4134

**DESIGN AND IMPLEMENTATION OF NONLINEAR
FORCE CONTROLLERS FOR FRICTION STIR WELDING
PROCESSES (PREPRINT)**

Xin Zhao, Prabhanjana Kalya, Robert G. Landers, and K. Krishnamurthy
University of Missouri Rolla

FEBRUARY 2009

Approved for public release; distribution unlimited.

See additional restrictions described on inside pages

STINFO COPY

**AIR FORCE RESEARCH LABORATORY
MATERIALS AND MANUFACTURING DIRECTORATE
WRIGHT-PATTERSON AIR FORCE BASE, OH 45433-7750
AIR FORCE MATERIEL COMMAND
UNITED STATES AIR FORCE**

REPORT DOCUMENTATION PAGE				<i>Form Approved</i> OMB No. 0704-0188	
<p>The public reporting burden for this collection of information is estimated to average 1 hour per response, including the time for reviewing instructions, searching existing data sources, gathering and maintaining the data needed, and completing and reviewing the collection of information. Send comments regarding this burden estimate or any other aspect of this collection of information, including suggestions for reducing this burden, to Department of Defense, Washington Headquarters Services, Directorate for Information Operations and Reports (0704-0188), 1215 Jefferson Davis Highway, Suite 1204, Arlington, VA 22202-4302. Respondents should be aware that notwithstanding any other provision of law, no person shall be subject to any penalty for failing to comply with a collection of information if it does not display a currently valid OMB control number. PLEASE DO NOT RETURN YOUR FORM TO THE ABOVE ADDRESS.</p>					
1. REPORT DATE (DD-MM-YY) February 2009		2. REPORT TYPE Journal Article Preprint		3. DATES COVERED (From - To) 01 February 2009 – 01 February 2009	
4. TITLE AND SUBTITLE DESIGN AND IMPLEMENTATION OF NONLINEAR FORCE CONTROLLERS FOR FRICTION STIR WELDING PROCESSES (PREPRINT)				5a. CONTRACT NUMBER FA8650-04-C-5704	
				5b. GRANT NUMBER	
				5c. PROGRAM ELEMENT NUMBER 78011F	
6. AUTHOR(S) Xin Zhao (Cummins) Prabhanjana Kalya, Robert G. Landers, and K. Krishnamurthy (University of Missouri)				5d. PROJECT NUMBER 2865	
				5e. TASK NUMBER 25	
				5f. WORK UNIT NUMBER 25100000	
7. PERFORMING ORGANIZATION NAME(S) AND ADDRESS(ES) University of Missouri Rolla 1870 Miner Circle Rolla, MO 65409-0970				8. PERFORMING ORGANIZATION REPORT NUMBER	
Cummins HHP Diesel Electronic Controls 2851 State Street Columbus, IN 47201					
9. SPONSORING/MONITORING AGENCY NAME(S) AND ADDRESS(ES) Air Force Research Laboratory Materials and Manufacturing Directorate Wright-Patterson Air Force Base, OH 45433-7750 Air Force Materiel Command United States Air Force				10. SPONSORING/MONITORING AGENCY ACRONYM(S) AFRL/RXLMP	
				11. SPONSORING/MONITORING AGENCY REPORT NUMBER(S) AFRL-RX-WP-TP-2009-4134	
12. DISTRIBUTION/AVAILABILITY STATEMENT Approved for public release; distribution unlimited.					
13. SUPPLEMENTARY NOTES PAO Case Number and clearance date: 88ABW-2008-1141, 26 November 2008. This work was funded in whole or in part by Department of the Air Force contract F8650-04-C-5704. The U.S. Government has for itself and others acting on its behalf an unlimited, paid-up, nonexclusive, irrevocable worldwide license to use, modify, reproduce, release, perform, display, or disclose the work by or on behalf of the U.S. Government.					
14. ABSTRACT In Friction Stir Welding (FSW) processes, force control can be used to achieve good welding quality. This paper presents the systematic design and implementation of FSW force controllers. The axial and path forces are modeled as nonlinear functions of the FSW process parameters (i.e., plunge depth, tool traverse rate, and tool rotation speed). Equipment models, which include communication delays, are constructed to relate the commanded and measured actuator signals. Based on the dynamic process and equipment models, nonlinear feedback controllers for the axial and path forces are designed using the Polynomial Pole Placement technique. The controllers are implemented in a Smith Predictor–Corrector structure to compensate for the inherent equipment communication delays and the controller parameters are tuned to achieve the best closed loop response possible given equipment limitations. In the axial force controller implementation, a constant axial force is maintained, even when gaps are encountered during the welding process.					
15. SUBJECT TERMS Friction Stir Welding, Feedback Control, Polynomial Pole Placement, Smith Predictor–Corrector					
16. SECURITY CLASSIFICATION OF:			17. LIMITATION OF ABSTRACT: SAR	18. NUMBER OF PAGES 42	19a. NAME OF RESPONSIBLE PERSON (Monitor) Todd J. Turner 19b. TELEPHONE NUMBER (Include Area Code) N/A
a. REPORT Unclassified	b. ABSTRACT Unclassified	c. THIS PAGE Unclassified			

Design and Implementation of Nonlinear Force Controllers for Friction Stir Welding Processes

Xin Zhao

Cummins

HHP Diesel Electronic Controls

2851 State Street

Columbus, Indiana 47201

Prabhanjana Kalya, Robert G. Landers, and K. Krishnamurthy

Missouri University of Science and Technology

Mechanical and Aerospace Engineering Department

1870 Miner Circle, Rolla, Missouri 65409–0050, USA

{pk34b;landersr;kkrishna}@mst.edu

Abstract

In Friction Stir Welding (FSW) processes, force control can be used to achieve good welding quality. This paper presents the systematic design and implementation of FSW force controllers. The axial and path forces are modeled as nonlinear functions of the FSW process parameters (i.e., plunge depth, tool traverse rate, and tool rotation speed). Equipment models, which include communication delays, are constructed to relate the commanded and measured actuator signals. Based on the dynamic process and equipment models, nonlinear feedback controllers for the axial

and path forces are designed using the Polynomial Pole Placement technique. The controllers are implemented in a Smith Predictor–Corrector structure to compensate for the inherent equipment communication delays and the controller parameters are tuned to achieve the best closed loop response possible given equipment limitations. In the axial force controller implementation, a constant axial force is maintained, even when gaps are encountered during the welding process. In the path force controller implementation, a constant path force is maintained, even in the presence of gaps, and wormhole generation during the welding process is eliminated by regulating the path force.

Key Words: Friction Stir Welding, Feedback Control, Polynomial Pole Placement, Smith Predictor–Corrector

Nomenclature

- C – Controller transfer function
- d – Plunge depth (mm)
- d_c – Commanded plunge depth (mm)
- E – Error (kN)
- f – Frequency (Hz)
- f_d – Frequency of plunge depth equipment model validation experiments (Hz)
- f_s – Sampling frequency (Hz)
- f_ω – Frequency of tool rotation speed equipment model validation experiments (Hz)
- F_a – Axial force (kN)
- F_p – Path force (kN)

- F_r – Reference force (kN)
- g – Gap distance (mm)
- G – Plant transfer function
- G_a – Axial force control system gain margin (dB)
- G_m – Gain margin (dB)
- G_p – Path force control system gain margin (dB)
- H – Open loop transfer function
- H_{cl} – Closed loop transfer function
- i – Imaginary number $\sqrt{-1}$
- n – number of equipment delay periods
- P_a – Axial force control system phase margin ($degree$)
- P_m – Phase margin ($degree$)
- P_p – Path force control system phase margin ($degree$)
- S – Sensitivity transfer function
- T – Sampling period (sec)
- T_d – Average delay time (sec)
- U – Control signal (mm or rpm)
- v – Tool traverse rate (mm/s)
- Y_f – Filtered general force (kN)
- Y_m – Measured general force (kN)
- z – Forward shift operator
- ω – Tool rotation speed (rpm)
- ω_c – Commanded tool rotation speed (rpm)

Introduction

Friction Stir Welding (FSW) is a new solid state welding technology that has been used successfully in many joining applications. In FSW processes, a rotating non-consumable tool, consisting of a pin and shoulder, plunges into the part such that both the pin and shoulder are in contact with the part. The tool rotation induces gross material plastic deformation due to an elevated temperature field. The tool travels along, or across, the intersection of two parts after dwelling for a specified amount of time, and joins the parts as the tool leaves the processing zone. This technique has advantages in that it can join materials that are difficult to weld by conventional welding processes, such as 2000 and 7000 series aluminum alloys, and part distortion and residual stresses are low. The FSW process is also environmentally friendly since harmful gases are not generated during the process.

It is often desirable to regulate the forces that are produced in FSW processes since machine geometric errors, structural deflections, improper fixturing, changes in thermal boundary conditions, etc. can cause poor weld quality, such as internal and surface voids, if constant process parameters are utilized. Axial force control is often used to ensure the tool shoulder maintains proper contact with the part without digging in too deep and creating surface voids. Also, experimental results [1] revealed a relationship between the generation of void defects and the path force: when the path force is above a critical value, void defects are generated. This result suggests that a feedback path force controller can be designed to eliminate the generation of void defects during FSW processes. The normal force has not been associated with defect formation; thus, the axial and path forces will be regulated in this paper.

Many manufacturing operations may be improved by regulating the process forces (e.g.,

[2–6]); however, force control has not been extensively investigated in the open literature. Smith [7] presented illustrations of robotic FSW with a serial industrial robot IRB 7600 working in a force feedback control mode. Strombeck [8] gave welding examples using the parallel industrial robot RIFTEC 600 with force feedback control. Cook [9] investigated the relationship between the increment in plunge depth and the corresponding increment in the axial force and noted that a force controller stability problem could be caused by the transient response characteristics during the beginning welding stage. Most current axial force feedback control algorithms in FSW machines are proprietary and, to the author’s knowledge, no systematic design techniques are available in the literature.

The rest of this paper is organized as follows. First, equipment utilized in this study and noise filtering are described. Dynamic FSW process models for the axial and path forces and the equipment dynamic models are presented. Then, the detailed design procedure of the force controllers using the Polynomial Pole Placement method implemented in a Smith Predictor–Corrector structure is introduced. Lastly, experimental validation studies are conducted and discussed.

Experimental Platform

The FSW system (Figure 1) used to conduct the experiments in this paper consists of a six degree of freedom robot (ABB IRB 940 Tricept robot), a FSW spindle head, a six axis force/moment sensor, and an open architecture control system. The robot has three non parallel telescopic translational joints and three rotational joints, and is retrofitted with a FSW spindle head to provide the rotational tool motion. The FSW spindle head (Figure 2) has a rotational axis driven by a 10 hp Exlar SLM115–368 servo motor with a rotational speed range of ± 3000 rpm. The load capability

of the spindle is 9.0 *kN* along the tool axis and 4.5 *kN* in the radial direction. The six-axis force/moment sensor system (JR3 Inc. model 75E20S-M125A-A 6000N1150) provides measurements of the process loading: the forces in three orthogonal directions and moments about each direction. The output analog voltage signal ranges are ± 10.0 V. The rated sensor forces are 6 *kN* in the x and y-directions and 12 *kN* in the z-direction. The rated moments are 1,150 *N·m* about all three directions. The teach pendant is used to manually control and program the robot.

The IRB 940 Tricept robot uses an S4cPlus robot control unit with RAPID as the programming language. The high level language RAPID enables the operator to pre-program the processing sequence and control algorithms in simple text formats, upload the source programs to the control unit, and compile and execute the code. Figure 3 illustrates the basic structure and functional blocks of the program used for the experiments conducted in this paper. The program consists of the initialization routines, a main welding loop executing in real-time during the welding process, and data storage routines executed after the process is complete. An interrupt procedure with an interval of 0.1 *sec* is triggered to provide a constant frequency of data acquisition and process parameter outputs as soon as the main welding loop is entered. During the interrupt procedure, the sensor data (i.e., forces and measured process parameters) are collected and the output signals (i.e., commanded process parameters) are calculated. These output signals are sent to their respective amplifiers during the main welding loop and, after the main loop finishes, all collected sensor data are saved to the control unit hard disk.

The experimental data contains significant electrical noise. Therefore, a five-point moving average was empirically determined to provide good data filtering without significant signal delay and unduly taxing the system's limited computational bandwidth. The filtered force signal is

$$Y_f(i) = \frac{1}{5} (Y_m(i) + Y_m(i-1) + Y_m(i-2) + Y_m(i-3) + Y_m(i-4)) \quad (1)$$

where $Y_f(i)$ is the filtered force at the i^{th} iteration and $Y_m(i)$ is the measured force at the i^{th} iteration. After implementing the filter, the standard deviation of the steady state force data with constant process parameters decreases approximately 50%.

Process and Equipment Dynamic Modeling

There has been a substantial amount of work in detailed thermo–mechanical models for FSW processes [10–12]. However, these models are solved using finite difference or finite element techniques and the computational requirements limit their use for controller design and implementation. In this paper, the controller designs are based on empirical dynamic models of the FSW process for 6061–T6 aluminum alloy (composition by weight: 97.9% Al, 0.60% Si, 0.30% Cu, 1.0% Mg, and 0.20% Cr). Based on the work of Zhao *et al.* [13], the axial (F_a) and path (F_p) forces are developed using the Least Square and Recursive Least Square techniques and can be modeled as second and first order systems, respectively, with the plunge depth and tool rotation speed, respectively, as the input process parameters. Other factors can be treated as disturbances (e.g., fixturing) or are constant during the operation (e.g., material properties, tool geometry, travel and work angles). Given a sampling frequency of 10 Hz, the models are converted into the discrete time domain with a Zero–Order–Hold transformation and, respectively, are

$$F_a(z) = \frac{v^{0.0970} \omega^{-0.230} (0.136z - 0.108)}{z^2 - 0.846z + 5.99 \cdot 10^{-2}} d^{2.21}(z) \quad (2)$$

$$F_p(z) = \frac{2.20 \cdot 10^{-2} v^{0.999}}{z - 0.854} \omega^{-1.23}(z) \quad (3)$$

where F_a is the axial force, v is the tool traverse rate, ω is the tool rotation speed, d is the plunge depth, and F_p is the path force. Note the forces increase as the tool traverse rate increases and as the tool rotation speed decreases. Since the force decreases with increasing temperature, this is in

agreement with the results in [14] that found temperature increases as the tool traverse rate decreases and tool rotation speed increases.

Due to the dynamic characteristics of the actuators and the communication delays that exist between the processors handling the high and low level computations, a dynamic relationship exists between the commanded and measured process parameters. Given the nonlinear relationships between the axial force and plunge depth and between the path force and tool rotation speed, as shown in equations (2) and (3), respectively, the dynamic relationships between $d^{2.21}$ and $d_c^{2.21}$ and between $\omega^{-1.23}$ and $\omega_c^{-1.23}$ are modeled, where d_c is the commanded plunge depth, and ω_c is the commanded tool rotation speed. Step change experiments for these parameters are conducted to determine these relationships. Experimental results show these relationships can be described by a pure delay and a first order transient response. Figures 4 and 5 show experimental results for the plunge depth and tool rotation speed, respectively, for step changes in the commanded process parameters. The number of delay periods is visually observed and the model time constants and gains are estimated by the Recursive Least Square method. For each parameter, nine runs are conducted and, therefore, 36 transient response data sets are collected. Delay times and time constants for the plunge depth and tool rotation speed equipment models are shown in Figures 6 and 7, respectively. The gains for both models are unity.

Taking the average delay times and time constants, the dynamic relationships between the commanded and measured plunge depth and tool rotation speed, respectively, are

$$\frac{d^{2.21}(s)}{d_c^{2.21}(s)} = \frac{e^{-0.531s}}{0.151s + 1} \quad (4)$$

$$\frac{\omega^{-1.23}(s)}{\omega_c^{-1.23}(s)} = \frac{e^{-0.294s}}{0.114s + 1} \quad (5)$$

The standard deviations of the plunge depth and rotation speed delay times are $4.67 \cdot 10^{-2} \text{ sec}$ and $6.30 \cdot 10^{-2} \text{ sec}$, respectively, and the standard deviations of the plunge depth and tool rotation speed time constants are $5.70 \cdot 10^{-2} \text{ sec}$ and $5.59 \cdot 10^{-2} \text{ sec}$, respectively. The smaller standard deviations of the plunge depth delay time and time constant indicate that it has a more consistent dynamic response as compared to the tool rotation speed. Also, the results show that the tool rotation speed has a relatively smaller delay time compared to the plunge depth, which is due to the fact that the spindle rotation and the robot's motions are implemented on two different computational systems. Since the welding program operates at a sampling frequency of $f_s = 10 \text{ Hz}$, the number of delay periods can be calculated based on the average equipment model delay time T_d and f_s as $n = \text{round}(T_d / f_s)$. Thus, the plunge depth and tool rotation speed equipment models, respectively, in the discrete domain, using a Zero–Order–Hold transformation, are

$$\frac{d^{2,21}(z)}{d_c^{2,21}(z)} = \frac{0.484}{z - 0.516} z^{-5} \quad (6)$$

$$\frac{\omega^{-1,23}(z)}{\omega_c^{-1,23}(z)} = \frac{0.587}{z - 0.413} z^{-3} \quad (7)$$

A series of sinusoidal experiments are conducted to validate the plunge depth and tool rotational speed equipment models. The commanded plunge depth and tool rotation speed are $d_c = 4.318 + 0.127 \sin(2\pi f_d t)$ and $\omega_c = 1900 + 300 \sin(2\pi f_\omega t)$, respectively. The frequencies of the sinusoidal experiments are limited by the rate limits imposed on both plunge depth and tool rotation speed, which are empirically determined and are 0.2 mm/s and 1000 rpm/s , respectively. Therefore, the maximum frequencies for the plunge depth and tool rotation speed sinusoidal experiments, are 0.251 Hz and 0.531 Hz , respectively. Four frequencies for each parameter are selected within these ranges. The model Bode Diagrams and the measured magnitude ratios and

phase shifts are shown in Figures 8 and 9, respectively, for the plunge depth and tool rotation speed equipment dynamics.

The Bode Diagrams indicate the models fit the experimental results very well. The maximum differences between the plunge depth modeled and measured magnitudes and phase shifts are 0.145 dB and -8.70° , respectively. The maximum differences between the tool rotation speed modeled and measured magnitudes and phase shifts are 0.403 dB and 12.0° , respectively. The differences are due to the fact that the delay times in the discrete time models are rounded to integers based on the sampling rate, which is either smaller (for the plunge depth equipment model) or larger (for the tool rotation speed equipment model) as compared to the average delay times.

It should be noted that the equipment and process models are empirical. The equipment model is machine dependent and the process model depends on the specific tool material and geometry, fixturing conditions, and material type. To apply the force control methodology proposed in this paper on another machine and for another process, new equipment and process models would need to be developed.

Controller Design

In this section feedback controllers utilizing the Polynomial Pole Placement (PPP) technique are designed to regulate the axial and path forces at constant values. The controllers are implemented in a Smith Predictor–Corrector (SPC) structure to compensate for the inherent equipment communication delay. The two controllers have the same closed loop system block diagram, as shown in Figure 10. The parameter F_r is the reference force, F is the measured force, E is the error between the reference and measured forces, U is the control signal, C is the controller transfer function, G is the model force process transfer function, and n is the number of equipment delay

periods.

Since the sampling rate is $f_s = 10 \text{ Hz}$, the operating bandwidth is $0\text{--}5 \text{ Hz}$. The design procedure consists of the following steps:

1. Calculate process model's zeros and poles.
2. Select closed loop system poles based on results of Step 1.
3. Calculate controller transfer function using the PPP technique with Internal Model Principle (IMP) based on closed loop poles selected in Step 2.
4. Evaluate closed loop system's stability and robustness within operating bandwidth using stability margins and sensitivity function.

The above design procedure is iterative, and Steps 2–4 may need to be repeated according to the stability and robustness results and experimental investigations. Detailed design steps are discussed in the following sections for the axial and path force controller designs.

Axial Force Controller

The plant dynamic model is a combination of the axial force process and equipment dynamic models, given in equations (2) and (6), respectively, and is

$$G_0(z) = G(z)z^{-5} \quad (8)$$

where

$$G(z) = \frac{b(z)}{a(z)} = \frac{v^{0.0970} \omega^{-0.230} (6.21 \cdot 10^{-2} z - 4.97 \cdot 10^{-2})}{z^3 - 1.42z^2 + 0.566z + 5.18 \cdot 10^{-2}} \quad (9)$$

In the initial controller design, the inherent equipment communication delay is ignored and

$$C(z) = \frac{p(z)}{q(z)} \quad (10)$$

The closed loop transfer function is

$$\frac{F(z)}{F_r(z)} = \frac{p(z)b(z)}{q(z)a(z) + p(z)b(z)} \quad (11)$$

The desired closed loop characteristic polynomial is $\alpha(z)$; therefore, the following equation must hold

$$q(z)a(z) + p(z)b(z) = \alpha(z) \quad (12)$$

Given the plant transfer function in equation (9) and a specified closed loop characteristic polynomial, the coefficients of $p(z)$ and $q(z)$ can be determined by equating like coefficients in equation (12).

Plant Transfer Function Zeros and Poles

As shown in equation (9), $G(z)$ has one zero located at $8.01 \cdot 10^{-2}$ and three poles located at 0.516, 0.772, and 0.130. The first pole corresponds to a time constant of 0.151 *sec* and is due to the equipment dynamics. The second and third poles correspond to two first order responses with time constants of 0.387 and $4.90 \cdot 10^{-2}$ *sec*, respectively, and are due to the axial force process dynamics.

Closed Loop Pole Locations

The closed loop characteristic polynomial is 6th order. The initial choice for this polynomial is

$$\alpha(z) = (z - r_1)(z - r_2)R(z) \quad (13)$$

where r_1 and r_2 are two dominant poles, and $R(z)$ is a 4th order polynomial. Since the plant transfer function has three poles with different time constants, the polynomial $R(z)$ is manipulated to contain two poles at the origin and two poles that are identical to the two poles of $G(z)$ with the smallest time constants

$$R(z) = z^2(z - 0.516)(z - 0.130) \quad (14)$$

Substituting equations (13) and (14) into equation (12)

$$\begin{aligned} p(z)b(z) &= z^2(z - r_1)(z - r_2)(z - 0.516)(z - 0.130) \\ -q(z) &= (z - 0.772)(z - 0.516)(z - 0.130) \end{aligned} \quad (15)$$

Substituting equation (15) into equation (11)

$$\frac{F(z)}{F_r(z)} = \frac{z^2(z - r_1)(z - r_2) - q(z)(z - 0.772)}{z^2(z - r_1)(z - r_2)} \quad (16)$$

Equation (16) shows that by manipulating the pole locations of $\alpha(z)$, the order of the closed loop characteristic polynomial is reduced from 6 to 4. Another pole placement strategy is for $\alpha(z)$ to have one dominant pole and for $R(z)$ to contain the three poles of the plant transfer function, with the fourth pole located at the origin. However, an analysis revealed that the closed loop system based on this pole placement strategy had poor stability and robustness and, therefore, was not pursued. Generally the rise time of the closed loop system should have at least 4–10 sampling periods to maintain closed loop stability [15]. Since the sampling period is 0.1 sec, r_1 and r_2 are initially chosen as 0.936 and 0.819, respectively, which correspond to time constants of 1.5 sec and 0.5 sec, respectively. The parameter r_1 is tuned experimentally by decreasing its value, without inducing instability and r_2 is tuned to the value that minimizes the sensitivity of the closed loop system, as discussed in the following section. The final design values are $r_1 = 0.9131$ and $r_2 = 0.7386$, which correspond to time constants of 1.1 sec and 0.33 sec, respectively. Substituting r_1 , r_2 , and equation (14) into equation (13), the closed loop characteristic polynomial is

$$\alpha(z) = z^6 - 2.30z^5 + 1.81z^4 - 0.546z^3 + 4.53 \cdot 10^{-2} z^2 \quad (17)$$

For the experiments conducted in this paper, the reference force is constant; therefore, the denominator of the controller transfer function must contain the factor $z-1$ to ensure robust

tracking. Denoting $q(z) = q_2(z)(z-1)$ to ensure the controller has integral action to track constant references and reject constant disturbances, equation (12) is transformed into

$$\begin{aligned} q_2(z)(z-1)(z^3 - 1.42z^2 + 0.566z + 5.18 \cdot 10^{-2}) + p(z)(6.21 \cdot 10^{-2}z - 4.50 \cdot 10^{-2})v^{0.0970}\omega^{-0.230} \\ = z^6 - 2.30z^5 + 1.81z^4 - 0.546z^3 + 4.53 \cdot 10^{-2}z^2 \end{aligned} \quad (18)$$

Given that the system order is 3, for a proper controller to exist such that equation (18) is satisfied, the minimal orders of $p(z)$ and $q_2(z)$ are, respectively, 3 and 2. The controller coefficients are calculated by equating like coefficients of equation (18), and the controller transfer function is

$$C(z) = \frac{p(z)}{q(z)} = \frac{(1.18z^3 - 9.33 \cdot 10^{-2}z^2 - 0.351z + 4.47 \cdot 10^{-2})v^{-0.0970}\omega^{0.230}}{z^3 - 0.880z^2 - 7.77 \cdot 10^{-2}z - 4.29 \cdot 10^{-2}} \quad (19)$$

Note that the numerator is an explicit function of v and ω and, therefore, the controller inherently compensates for variations in the tool traverse rate and tool rotation speed.

Closed Loop System Stability and Robustness

Since the plant model contains modeling inaccuracies, the sensitivity function and the stability margins are checked during the design procedure to ensure the closed loop system has sufficient stability and robustness. For the closed loop system not implemented in the SPC structure, the sensitivity function is

$$S(z) = \frac{1}{1 + C(z)G(z)} \quad (20)$$

The sensitivity function can be interpreted as the ratio of the change in the closed loop transfer function to the change in the open loop transfer function [16]

$$\frac{d(H_{cl})}{H_{cl}} = S \frac{d(H)}{H} \quad (21)$$

where $H(z) = C(z)G(z)$ is the open loop transfer function and $H_{cl}(z) = H(z)(1 + H(z))^{-1}$ is the closed

loop transfer function. The sensitivity function $S(z)$ is used as a measure of the closed loop system sensitivity to noise, external disturbances, and modeling errors. Substituting $z = e^{iT}$, where T is the sampling period, i is the imaginary number, and f is the frequency, into equation (20) yields

$$S(e^{iT}) = \frac{1}{1 + C(e^{iT})G(e^{iT})} \quad (22)$$

The inverse of $|S(e^{iT})|$ is $|1 + C(e^{iT})G(e^{iT})|$, which represents the distance from a point of the Nyquist curve of the open loop transfer function $C(e^{iT})G(e^{iT})$ to the critical point -1 . To have good robustness and maintain stability against modeling errors, $|S(e^{iT})| < 2$ [15]. The value of $|S(e^{iT})|$ for $0 < f < 5$ Hz is plotted in Figure 11. The maximum value of the sensitivity function is 1.18; thus, the desired closed loop system meets the sensitivity requirement.

The gain and phase margins, respectively, are

$$G_m = 20 \log_{10} |H(i\omega_1)| \quad (23)$$

$$P_m = \angle H(i\omega_2) \quad (24)$$

where ω_1 is the phase crossover frequency where the phase is -180° and ω_2 is the magnitude crossover frequency where the magnitude of H is 1. The closed loop system is stable only if $G_m > 0$ and $P_m > 0$. Generally, $G_m > 6$ dB and $P_m > 30^\circ$ for the closed loop system to have sufficient robustness against modeling errors [17]. Figure 12 shows the Bode Diagram, including the magnitude and phase margins, which are 19.4 dB and 84.4° , respectively, and meet the stability margin requirements.

Implementation in Smith Predictor–Corrector Structure

The next step of the controller design is to implement the controller in a Smith Predictor–Corrector

(SPC) structure. The overall closed loop system diagram is shown in Figure 10 where $n = 5$ is the number of the equipment delay periods. The modified control law is

$$\begin{aligned} u(k) = & 0.879u(k-1) + 7.77 \cdot 10^{-2}u(k-2) + 4.29 \cdot 10^{-2}u(k-3) \\ & + 1.18v^{-0.0970} \omega^{0.230} [e(k) - e_1(k)] - 9.33 \cdot 10^{-2}v^{-0.0970} \omega^{0.230} [e(k-1) - e_1(k-1)] \\ & - 0.351v^{-0.0970} \omega^{0.230} [e(k-2) - e_1(k-2)] + 4.47 \cdot 10^{-2}v^{-0.0970} \omega^{0.230} [e(k-3) - e_1(k-3)] \end{aligned} \quad (25)$$

where

$$\begin{aligned} e_1(k) = & 1.42e_1(k-1) - 0.566e_1(k-2) + 5.18 \cdot 10^{-2}e_1(k-3) \\ & + 6.21 \cdot 10^{-2}v^{0.0970} \omega^{-0.230} [u(k-2) - u(k-7)] - 4.97 \cdot 10^{-2}v^{0.0970} \omega^{-0.230} [u(k-3) - u(k-8)] \end{aligned} \quad (26)$$

and $u(k) = d_c^{2.21}(k)$ is the control signal. The commanded plunge depth is determined using the nonlinear mapping $d_c(k) = u^{-2.21}(k)$. Due to the load capacity of the FSW robot and the possibility of tool breakage, control signal saturation is required for both the plunge depth and the rate of change of the plunge depth. The tool geometry restricts the range of the plunge depth: the tool shoulder must maintain contact with the plate's surface to ensure proper forging action and a plunge depth that is too deep generates excessive material flow away from the welding surface, creating surface voids. Since the pin length is 4.165 mm , the plunge depth is chosen to be in the range of 4.17 to 4.60 mm . Also, a rate limit of 0.20 mm/s is applied based upon the operator's experience. Magnitude and rate signal saturations are implemented within the controller program.

Path Force

The path force controller is also designed using the PPP technique with the application of the IMP. The plant transfer function $G_0(z)$, incorporating the path force process and rotational speed models, is

$$G_0(z) = G(z)z^{-3} \quad (27)$$

where

$$G(z) = \frac{b(z)}{a(z)} = \frac{1.29 \cdot 10^{-2} v^{0.999}}{z^2 - 1.27z + 0.353} \quad (28)$$

The poles are located at 0.854 and 0.413. The first pole is due to the path force process model dynamics and the second pole is due to the equipment model dynamics. The operating bandwidth is again 5 Hz.

The order of the path force dynamic model is 2; therefore, the order of the closed loop characteristic polynomial is 4. Similar to the axial force controller design, the closed loop characteristic polynomial is manipulated to contain the factors of $a(z)$ so that the order of the closed loop transfer function is reduced. An initial design of $\alpha(z)$ is

$$\alpha(z) = (z - r_0)(z - r_1)(z - r_2)z \quad (29)$$

where r_0 is the dominant pole and r_1 and r_2 are identical to the plant transfer function poles. The time constant of the dominant pole is set to 1.2 sec, based on experimental results, so that the closed loop system response is fast and the system still has sufficient stability and robustness.

Therefore, $r_0 = 0.926$. Substituting r_0 , r_1 , and r_2 into equation (29)

$$\alpha(z) = z^4 - 2.19z^3 + 1.52z^2 - 0.324z \quad (30)$$

The controller transfer function is

$$C(z) = \frac{p(z)}{q(z)} = \frac{(6.19z^2 - 7.84z + 2.18)v^{-0.999}}{z^2 - 0.920z - 8.00 \cdot 10^{-2}} \quad (31)$$

The controller is an explicit function of v and, therefore, inherently compensates for variations in the tool traverse rate. The closed loop design is also evaluated by computing the sensitivity function and stability margins. Figure 11 shows the value of sensitivity function in the range of $0 < f < 5$ Hz, and the maximum value is 1.10. Figure 12 shows the Bode Diagram, including the

stability margins. The magnitude and phase margins are 22.6 dB and 83.9°, respectively. Therefore, the requirements for both sensitivity and stability margins are satisfied.

Similar to the axial force controller design, the path force controller is implemented in a Smith Predictor–Corrector structure and the control law is

$$\begin{aligned} u(k) = & 0.920u(k-1) + 8.00 \cdot 10^{-2}u(k-2) + 6.19v^{-0.999} [e(k) - e_1(k)] \\ & - 7.84v^{-0.999} [e(k-1) - e_1(k-1)] + 2.18v^{-0.999} [e(k-2) - e_1(k-2)] \end{aligned} \quad (32)$$

where

$$e_1(k) = 1.27e_1(k-1) - 0.355e_1(k-2) + 1.29v^{0.999} [u(k-2) - u(k-5)] \quad (33)$$

and $u(k) = \omega_c^{-1.23}(k)$ is the control signal. The commanded tool rotation speed is determined using the nonlinear mapping $\omega_c(k) = u^{1.23}(k)$.

Experimental Validation

In this section, lap welding experiments are conducted to validate the performances of the axial and path force controllers. Figure 13 shows the lap welding experimental setup.

Axial Force

In the first set of axial force controller validation experiments, the tool traverse rate and tool rotation speed are constant and the reference axial force is changed twice in a step–wise manner during the experiment. The reference force is F_{r1} for the first third of the welding distance, F_{r2} for the second third, and F_{r3} for the last third. Five experimental tests with different combinations of tool traverse rate and tool rotation speed are conducted to validate the controller’s performance. Given the specific tool traverse rate, tool rotation speed, and the pre–selected plunge depth range,

the reference force values are adjusted according to experimental results so that the tool shoulder maintains proper contact with the plate surface and good weld quality is obtained (i.e., surface voids are not created). Table 1 shows the process parameter combinations and reference axial forces for the five experiments.

Figure 14 shows the experimental results for the third test and Table 1 gives the averages and standard deviations of the axial forces during the three steady-state portions of each test. The measured axial forces tracked the reference axial forces well for each experiment. The standard deviations are below 1% of the averages' magnitudes, except for the second steady-state of the fourth test, where the large tracking error is caused by a sudden disturbance, which could be caused by material defects, fixturing issues, etc. It is also observed that during the steady states where the axial forces are constant, the plunge depth has significant variations. These variations are mainly due to the machine's geometric error. Other factors that contribute to these variations are the non-uniformity in the plate's flatness and material properties, structural deflections, non-uniformity in the fixturing, and changes in the thermal boundary conditions as the tool travels from one end of the plate to the other. The controller is able to compensate for these effects and maintain a constant axial force.

The next set of experiments explores the effects skin-to-skin and substructure gaps have on the axial force controller. A four-piece experimental setup, illustrated in Figure 15, is utilized for these experiments and two plates, separated by shims of constant thickness, are placed on the top, forming a skin-to-skin gap. Two plates, also separated by shims with the same thickness, are placed on the bottom, forming a substructure gap. The welding start and end locations are selected such that the welding path goes across both gaps. Two groups of experiments are conducted to analyze the force controller performance: tests 1–6 utilize axial force control for different

combinations of tool traverse rate and tool rotation speed and tests 7–12 utilize constant plunge depth for the corresponding combinations of tool traverse rate and tool rotation speed. The reference axial force for each test was selected, based on experimental investigations, such that the tool shoulder maintained contact with the plate surface and surface voids were not created. The plunge depth for each run in the second group was computed from the axial force model, given the combination of reference force, tool traverse rate, and tool rotation speed.

Figure 16 shows the experimental results for tests 4 (axial force control) and 10 (constant plunge depth). In this figure, the top and middle subplots show the axial force control results, and the bottom subplot shows the corresponding constant plunge depth results. On each subplot, the three dotted lines on the left side of the figure indicate the times when the sides and center of the tool shoulder engage and leave the substructure gap, and the three dotted lines on the right side of the figure indicate when the sides and center of the tool shoulder engage and leave the skin-to-skin gap. It is observed that when the force controller is implemented, a constant axial force is maintained at the reference value during the welding process even when skin-to-skin and substructure gaps are encountered. When the plunge depth was constant, the axial force decreases when crossing both skin-to-skin and substructure gaps. This is due the fact that the tool encounters less material as it crosses the gaps and thus, less axial force is applied to the tool.

The average axial forces and standard deviations for the two groups of experiments are shown in Table 2. It is observed that for the tests with a lower tool traverse rate the difference between the axial force standard deviations of experiments with axial force control and experiments with constant plunge depth are larger as compared to those with a higher tool traverse rate. One explanation is that when the tool traverse rate is lower, the time period for the tool to travel across the gap is longer, which causes a greater decrease in axial force and, therefore, the improvement

provided by implementing the controller is greater. The axial force control experiments have much better performance as compared to the corresponding constant plunge depth experiments. It is observed that the measured axial force has greater variation from the desired axial force when the plunge depth is constant. This is due to the existence of gaps, variations in the thermal boundary and fixturing conditions, and axial force modeling errors.

The third set of axial force validation experiments is designed to test the controller's performance when welding along skin-to-skin gaps. Figure 17 shows the experimental setup. Four gap sizes are investigated: constant gap of 0.381 mm , constant gap of 0.762 mm , tapered gap that increases linearly from 0.381 mm to 0.762 mm , and no gap. The process parameters are identical to test #3 in Table 1 where the controller has the best performance, the weld quality from visual inspection is very good, and the reference axial force is 3.00 kN . Figure 18 shows the experimental results when a variable gap is encountered, and Table 3 gives the axial force averages and standard deviations during the three steady state portions of each test. The results show that the axial force controller also works well when welding along a gap, and the axial force is not significantly affected by the existence of gaps up to 0.762 mm in width. The tracking precision is similar to the experiments where no gaps are present and the experiments where the tool crosses skin-to-skin and substructure gaps.

Path Force

In the first set of path force controller validation experiments, the controller is implemented to track constant reference path forces and the plunge depth and tool traverse rate are constant. According to the path force model, the plunge depth does not affect the force significantly; therefore, a plunge depth of 4.20 mm is selected, based upon experimental observations, to ensure

the tool shoulder maintains contact with the plate and surface voids are not created during the welding process. Three experiments are conducted with different traverse rates and reference force levels such that the shoulder maintains contact with the plate and good weld quality is obtained (i.e., surface voids are not created). The reference path force changes from the high (F_{r1}) to the low (F_{r2}) value in a step-wise manner in the middle of the weld. Figure 19 shows the experimental results for the second test and Table 4 shows the process parameters and the path force averages and standard deviations during the two steady-state portions for each test. The results show the controller tracks the reference path force well for all three tests. However, compared to the axial force controller experiments, the path force has greater variation. At least two factors contribute to this phenomenon: 1) the path force has a much lower magnitude (0.1–0.4 kN) than the axial force (2.5–3.5 kN) and, therefore, the signal to noise ratio is much less and 2) the path force dynamic model is less accurate as compared to the axial force dynamic model [13].

The second set of path force validation experiments is designed to examine the controller's performance when welding along skin-to-skin gaps. The experimental setup is shown in Figure 17. Four gap sizes are examined: a constant gap of 0.381 mm , a constant gap of 0.762 mm , a tapered gap increasing linearly from 0.381 to 0.762 mm , and no gap. The reference path force experiences a step-wise change from F_{r1} to F_{r2} in the middle of the weld. A constant traverse rate of 3.2 mm/s , for which the path force has the smallest standard deviation when tracking the lowest force, is applied for all three experiments. Due to the gap, a constant plunge depth of 4.25 mm , 0.05 mm deeper as compared to the experiments without gaps, is applied to obtain the same path force level. Figure 20 shows the experimental results for test 3 and Table 5 shows the tracking performance for each test. The results show that the steady-state averages and standard deviations are similar to those obtained in test 3 of the first set of experiments, which has the same traverse

rate and reference force. This indicates the path force controller also works well when welding along skin-to-skin gaps and the path force is not significantly affected by the presence of these types of gaps.

The third set of experiments is designed to demonstrate the ability of the path force controller to eliminate the generation of wormholes during the welding process. In this experiment, the plunge depth and traverse rate are 4.20 mm and 3.20 mm/s, respectively, and the initial tool rotation speed is 900 rpm. During the first 20 seconds, the controller is not implemented and after 20 seconds, the controller is activated to regulate the path force at a reference value of 0.22 kN. The reference path force is selected so a good weld will be obtained without wormholes or the creation of surface voids. The experimental results are shown in Figure 21. It is observed that the implementation of the controller maintained the path force at a constant value. In the steady state with force control (5.0–20.0 sec), the average value of path force is 0.215 kN and the standard deviation is $7.95 \cdot 10^{-3}$ kN. Figure 22 shows pictures of the weld cross-sections during the steady-states both with path force control (26.5–48.0 sec) and with constant tool rotation speed (20.0–48.0 sec). It is observed that with the implementation of the path force controller, void defects, as shown in subplot (b), are eliminated, as shown in subplot (a).

Summary and Conclusions

Model-based, nonlinear axial and path force controllers were designed using the Polynomial Pole Placement technique with the Internal Model Principle for friction stir welding processes. The models consisted of equipment models, which were developed in this paper, and process models, that were taken from the literature. The controllers were implemented in a Smith Predictor-Corrector structure to compensate for inherent equipment communication delays. A

detailed design procedure was introduced and several experiments were conducted to validate the controllers' performance.

Experimental results validated the developed equipment models. The axial force controller was experimentally shown to perform well when tracking a constant axial force, even when gaps were encountered across and along the weld path. The path force controller was also experimentally shown to be able to track a constant path, even when gaps were encountered along the weld path. However, the tracking precision is relatively lower for the path force controller, as compared to the axial force controller, due to the smaller signal to noise ratio and modeling inaccuracies that exist in the path force model. One experiment showed that the wormhole defect during the welding process can be eliminated by the implementation of the path force controller.

Acknowledgement

The authors wish to acknowledge the financial support for this work from the Missouri S&T Center for Aerospace Manufacturing Technologies (Air Force Research Laboratory contract FA8650-04-C-5704) and the technical support of colleagues at Missouri S&T, the Boeing Company, and the Air Force Research Laboratory.

References

- [1] Kalya, P., 2007, *Modeling and Control of Friction Stir Welding*, Doctoral Dissertation, University of Missouri–Rolla, Department of Mechanical and Aerospace Engineering, Rolla, Missouri.
- [2] Chen, L., Stango, R.J., and Cariapa, V., 2001, “A Force–Control Model for Edge–Deburring with Filamentary Brush,” *ASME Journal of Manufacturing Science and Engineering*, Vol. 123, No.

3, pp. 528–532.

[3] Viswanathan, V., Kinsey, B., and Cao, J., 2003, “Experimental Implementation of Neural Network Springback Control for Sheet Metal Forming,” *ASME Journal of Engineering Materials and Technology*, Vol. 125, No. 2, pp. 141–147.

[4] Liang, S.Y., Hecker, R.L., and Landers, R.G., 2004, “Machining Process Monitoring and Control: The State-of-the-Art,” *ASME Journal of Manufacturing Science and Engineering*, Vol. 126, No. 2, pp. 297–310.

[5] Xu, C. and Shin, Y.C., 2007, “Control of Cutting Force for Creep-Feed Grinding Processes using a Multi-Level Fuzzy Controller,” *ASME Journal of Dynamic Systems, Measurement, and Control*, Vol. 129, No. 4, pp. 480–492.

[6] Mason, M.S., Huang, T., Landers, R.G., Leu, M.C., and Hilmas, G.E., 2006, “Freeform Extrusion of High Solids Loading Ceramic Slurries, Part II: Extrusion Process Control,” *Seventeenth Annual Solid Freeform Fabrication Symposium*, Austin, Texas, August 14–16.

[7] Smith, C.B., Hinrichs, J.F., and Crusan, W.A., 2003, “Robotic Friction Stir Welding: the State of the Art,” *Proceedings of the 4th International Symposium of Friction Stir Welding*, Park City, Utah, May 14–16.

[8] Von Strombeck, A., Schilling, C., and Dos Santos, J.F., 2000, “Robotic Friction Stir Welding – Tool, Technology and Applications,” *Proceedings of the 2nd International Symposium of Friction Stir Welding*, Gothenburg, Sweden, June 26–28.

[9] Cook, G.E., Smart, H.B., Mitchell, J.E., Strauss, A.M., and Crawford, R., 2003, “Controlling Robotic Friction Stir Welding,” *Welding Journal*, Vol. 82, No. 6, pp. 28–34.

[10] Chao, Y.J., Qi, X., and Tang, W., 2003, “Heat Transfer in Friction Stir Welding – Experimental and Numerical Studies,” Vol. 125, No. 1, pp. 138–145.

- [11] Ulysse, P., 2002, “Three–Dimensional Modeling of the Friction Stir Welding Process,” *International Journal of Machine Tools and Manufacture*, Vol. 42, No. 14, pp. 1549–1557.
- [12] Heurtier, P., Jones, M., Desrayaud, C., Driver, J., Montheillet, F., and Allehaux, D., 2006, “Mechanical and Thermal Modeling of Friction Stir Welding,” *Journal of Materials Processing Technology*, Vol. 171, No. 3, pp. 348–357.
- [13] Zhao, X., Kalya, P., Landers, R.G., and Krishnamurthy, K., 2007, “Empirical Dynamic Modeling of Friction Stir Welding Processes,” *ASME International Conference on Manufacturing Science and Engineering*, Atlanta, Georgia, October 15–18.
- [14] Arbegast, W.J. and Hartley, P.J., 1998, “Friction Stir Weld Technology Development at Lockheed Martin Michoud Space System—An Overview,” *Proceedings of the Fifth International Conference on Trends in Welding Research*, Pine Mountain, Georgia, June 1–5, pp. 541–546.
- [15] Åström, K.J. and Wittenmark, B., 1997, *Computer–Controlled Systems—Theory and Design*, 3rd ed., pp. 110–111 and 183–185, Prentice Hall, Upper Saddle River, New Jersey.
- [16] De Silva, C.W., 2004, *Mechatronics—An Integrated Approach*, pp. 1032–1034, CRC Press LLC, Boca Raton, Florida.
- [17] Ogata, K., 2002, *Modern Control Engineering*, 4th ed., Prentice Hall, Upper Saddle River, New Jersey.

Table 1: Axial Force Controller Tracking Performance during Steady-State. F_{1ss} , F_{2ss} , and F_{3ss} are Steady-State Axial Forces for First, Second, and Third, respectively, Sections.

Test	v (mm/s)	ω (rpm)	F_{1ss} [F_{r1}] (kN)	$\sigma(F_1)$ (kN)	F_{2ss} [F_{r2}] (kN)	$\sigma(F_2)$ (kN)	F_{3ss} [F_{r3}] (kN)	$\sigma(F_3)$ (kN)
1	3.2	1600	3.46 [3.45]	$2.75 \cdot 10^{-2}$	3.65 [3.65]	$1.10 \cdot 10^{-2}$	3.54 [3.55]	$2.76 \cdot 10^{-2}$
2	3.2	2100	3.27 [3.25]	$1.76 \cdot 10^{-2}$	3.46 [3.45]	$1.84 \cdot 10^{-2}$	3.34 [3.35]	$2.01 \cdot 10^{-2}$
3	2.0	1600	3.01 [3.00]	$9.10 \cdot 10^{-3}$	3.21 [3.20]	$1.13 \cdot 10^{-2}$	3.11 [3.10]	$1.36 \cdot 10^{-2}$
4	2.0	2100	2.71 [2.70]	$2.15 \cdot 10^{-2}$	2.90 [2.90]	$3.87 \cdot 10^{-2}$	2.80 [2.80]	$1.63 \cdot 10^{-2}$
5	2.6	1900	2.92 [2.90]	$2.17 \cdot 10^{-2}$	3.11 [3.10]	$1.33 \cdot 10^{-2}$	3.00 [3.00]	$1.77 \cdot 10^{-2}$

Table 2: Tracking Performance for Axial Force Controller and Constant Plunge Depth when Welding across Gaps. F_{ss} is Steady-State Axial Force.

v (mm/s)	ω (rpm)	F_r (kN)	Constant Axial Force			Constant Plunge Depth		
			Test	F_{ss} (kN)	$\sigma(F_1)$ (kN)	Test	F_{ss} (kN)	$\sigma(F_2)$ (kN)
3.2	1600	3.40	1	3.41	$3.40 \cdot 10^{-2}$	7	3.37	$4.46 \cdot 10^{-2}$
3.2	2100	3.30	2	3.31	$3.92 \cdot 10^{-2}$	8	3.55	$6.73 \cdot 10^{-2}$
2.0	1600	3.15	3	3.16	$2.90 \cdot 10^{-2}$	9	3.41	$6.06 \cdot 10^{-2}$
2.0	2100	2.95	4	2.95	$2.18 \cdot 10^{-2}$	10	3.18	$7.89 \cdot 10^{-2}$
2.6	1900	3.25	5	3.25	$3.89 \cdot 10^{-2}$	11	3.12	$5.14 \cdot 10^{-2}$
3.2	2100	3.30	6	3.31	$1.69 \cdot 10^{-2}$	12	3.19	$6.85 \cdot 10^{-2}$

Table 3: Tracking Performance for Axial Force Controller when Welding along Gaps ($v = 2.0$ mm/s, $\omega = 1600$ rpm, and $F_r = 3.00$ kN). F_{ss} is Steady-State Axial Force.

Test	g (mm)	F_{ss} (kN)	$\sigma(F)$ (kN)
1	0.381	3.01	$1.54 \cdot 10^{-2}$
2	0.762	3.00	$1.55 \cdot 10^{-2}$
3	0.381 \rightarrow 0.762	3.01	$1.70 \cdot 10^{-2}$
4	0	3.00	$2.25 \cdot 10^{-2}$

Table 4: Path Force Controller Tracking Performance during Steady-State ($d = 4.20$ mm). F_{1ss} and F_{2ss} are Steady-State Path Forces for First and Second, respectively, Sections.

Test	v (mm/s)	F_{r1} (kN)	F_{r1ss} (kN)	$\sigma(F_1)$ (kN)	F_{r2} (kN)	F_{r2ss} (kN)	$\sigma(F_2)$ (kN)
1	2.0	0.16	0.159	$1.29 \cdot 10^{-2}$	0.13	0.131	$0.727 \cdot 10^{-2}$
2	2.6	0.19	0.191	$1.18 \cdot 10^{-2}$	0.16	0.162	$0.601 \cdot 10^{-2}$
3	3.2	0.23	0.236	$1.34 \cdot 10^{-2}$	0.20	0.202	$0.592 \cdot 10^{-2}$

Table 5: Tracking Performance of Path Force Controller when Welding along Gaps ($d = 4.25$ mm and $v = 3.2$ mm/s). F_{1ss} and F_{2ss} are Steady-State Path Forces for First and Second, respectively, Sections.

Test	g (mm)	F_{r1} (kN)	F_{1ss} (kN)	$\sigma(F_1)$ (kN)	F_{r2} (kN)	F_{2ss} (kN)	$\sigma(F_2)$ (kN)
1	0.381	0.23	0.232	$7.37 \cdot 10^{-3}$	0.20	0.200	$8.38 \cdot 10^{-3}$
2	0.762	0.23	0.228	$8.36 \cdot 10^{-3}$	0.20	0.201	$6.44 \cdot 10^{-3}$
3	0.381→0.762	0.23	0.237	$1.06 \cdot 10^{-2}$	0.20	0.204	$6.36 \cdot 10^{-3}$
4	0	0.23	0.230	$8.61 \cdot 10^{-3}$	0.20	0.202	$6.63 \cdot 10^{-3}$

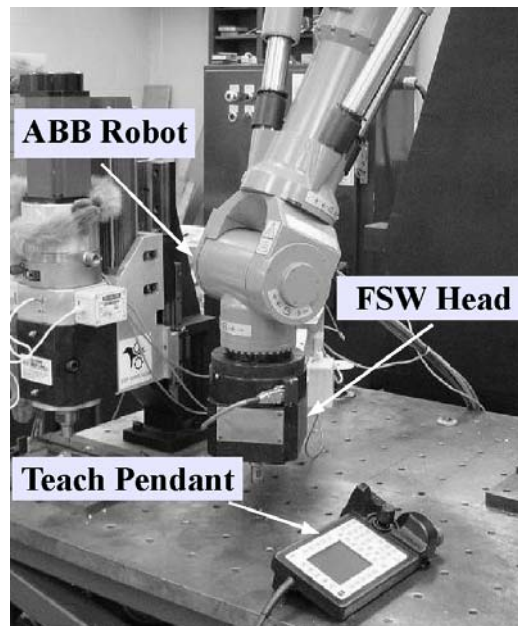


Figure 1: Friction Stir Welding System.

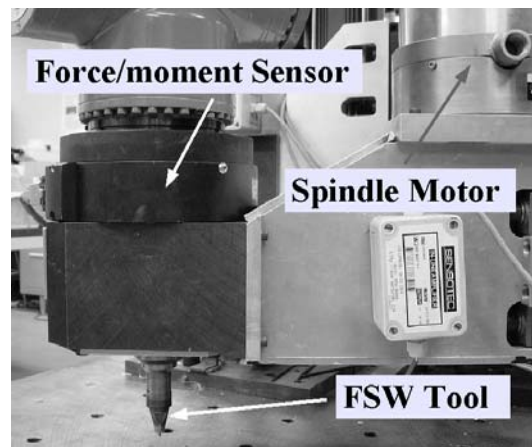


Figure 2: FSW Head with Tool and Six-Axis Force/Moment Sensor.

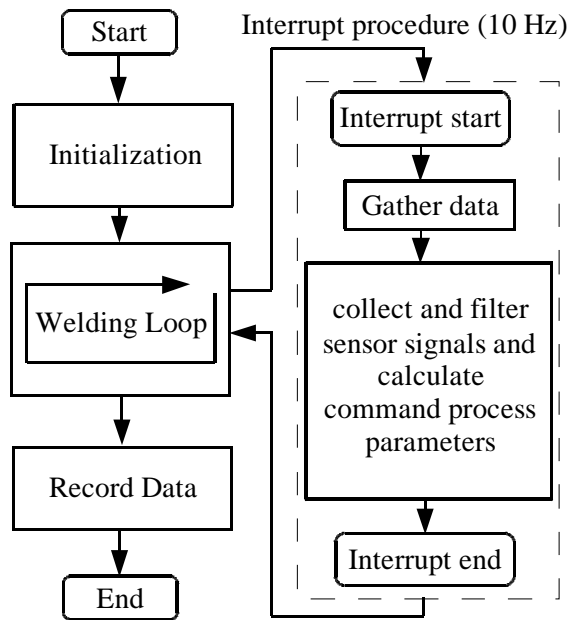


Figure 3: Robotic Friction Stir Welding Force Control Program Functional Block Structure.

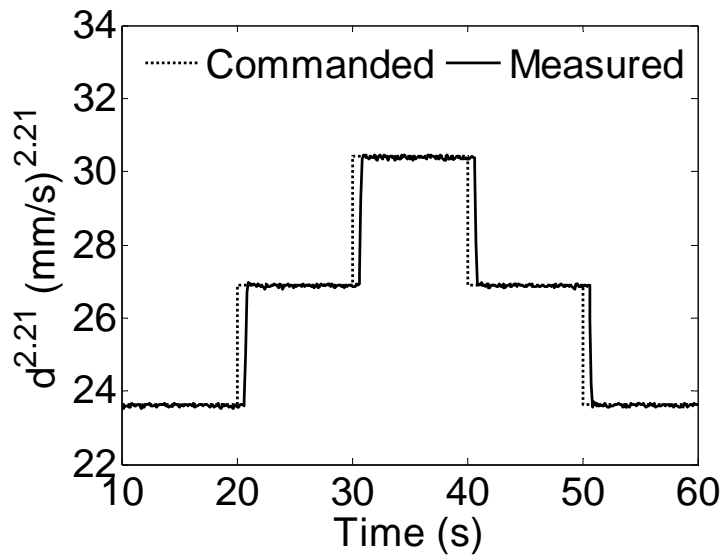


Figure 4: Commanded and Measured Plunge Depth Responses.

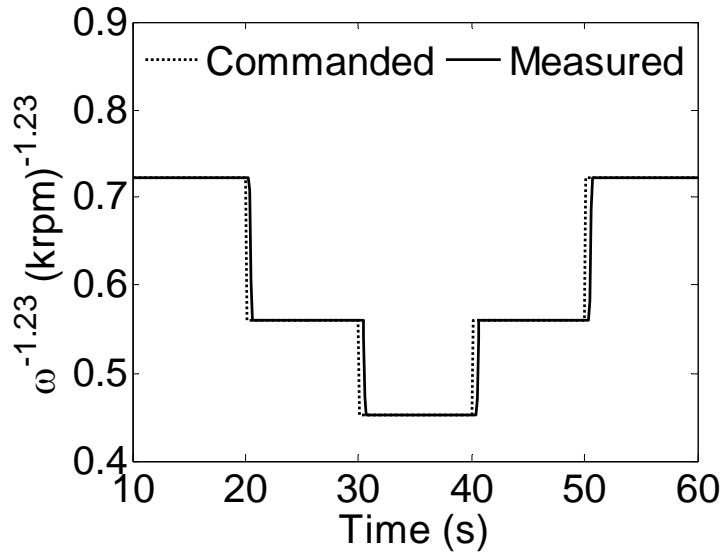


Figure 5: Commanded and Measured Tool Rotation Speed Responses.

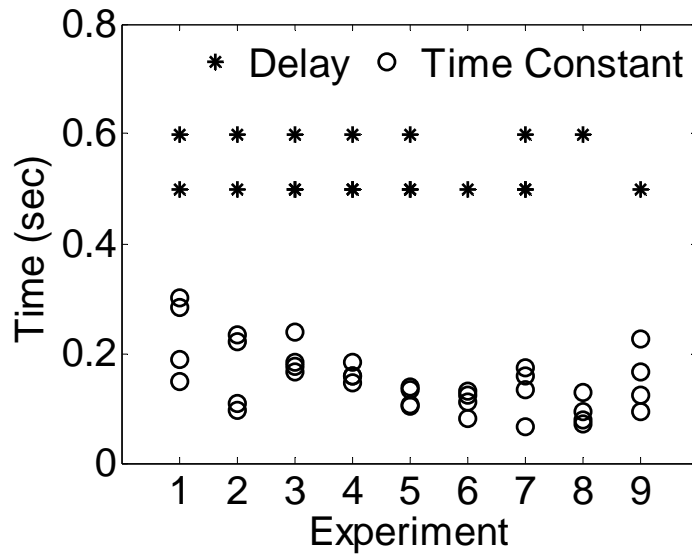


Figure 6: Plunge Depth Equipment Model Delays and Time Constants.

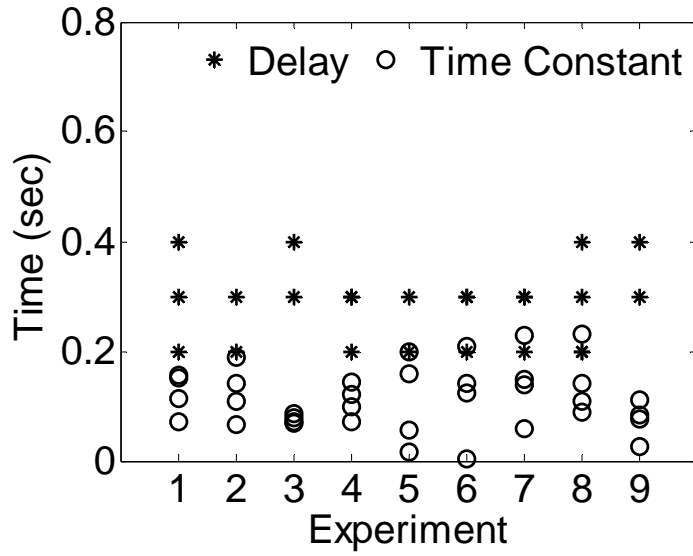


Figure 7: Tool Rotation Speed Equipment Model Delays and Time Constants.

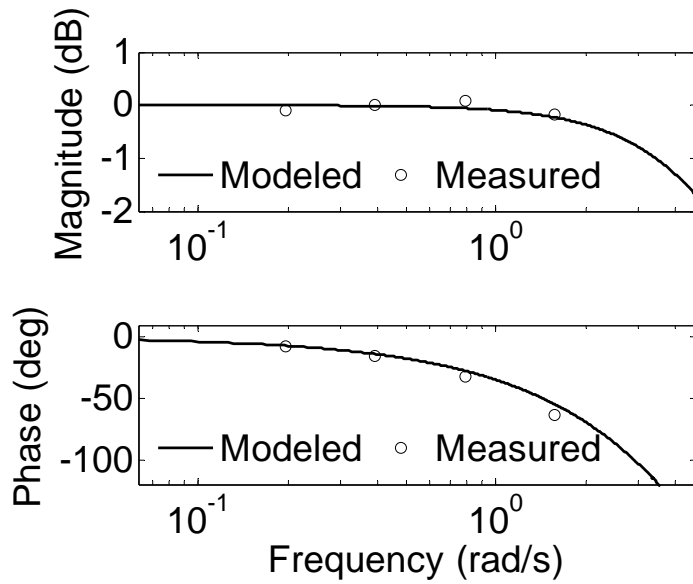


Figure 8: Plunge Depth Equipment Modeled and Measured Bode Diagrams.

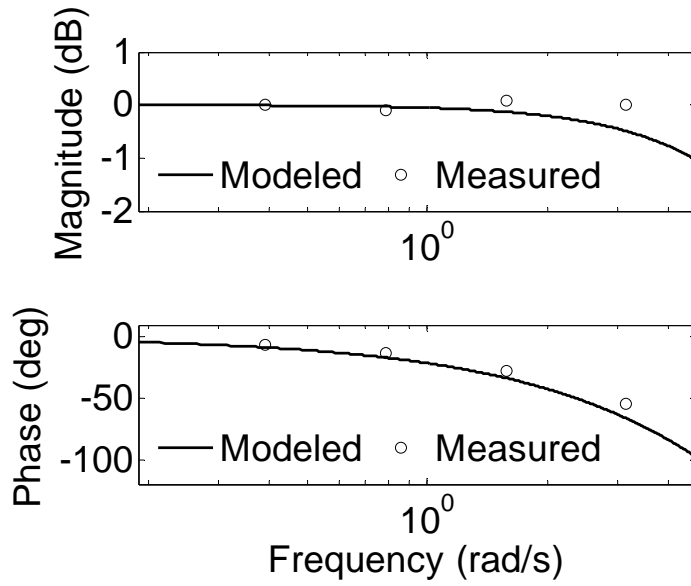


Figure 9: Tool Rotation Speed Equipment Modeled and Measured Bode Diagrams.

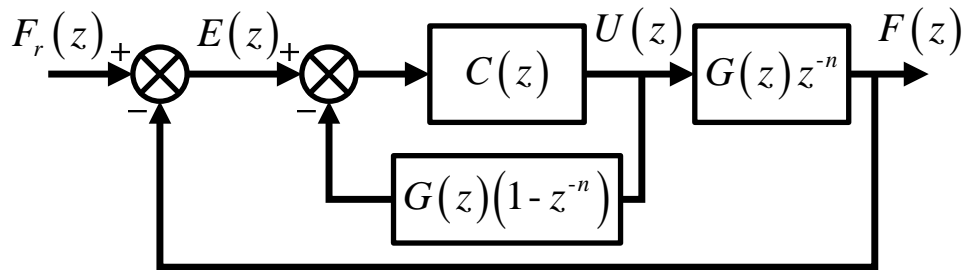


Figure 10: Closed Loop Force Control System Block Diagram.

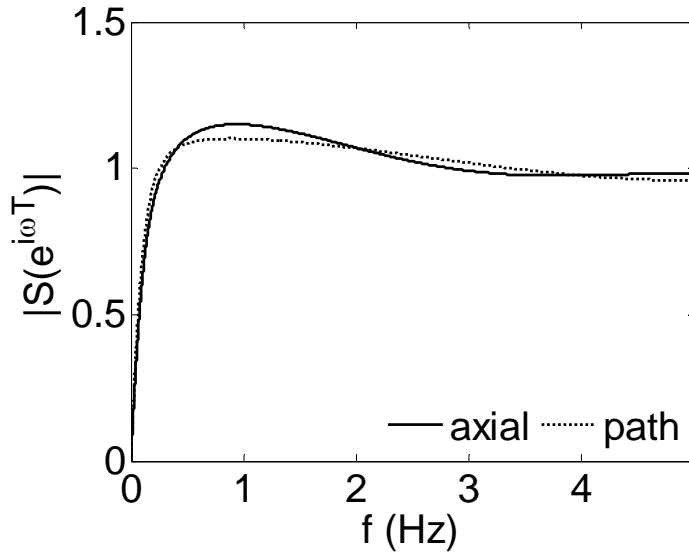


Figure 11: Axial and Path Force Closed Loop System Sensitivity Functions.

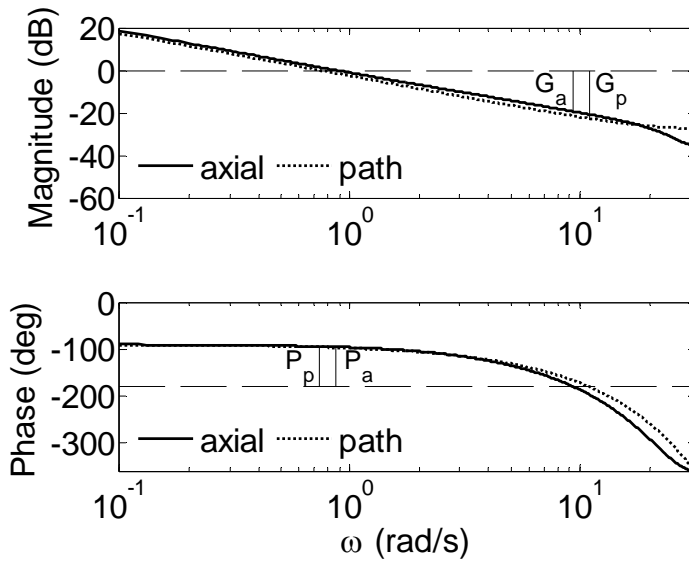


Figure 12: Axial Force Control System Bode Diagrams and Stability Margins ($G_a = 19.4$ dB and $P_a = 84.4^\circ$) and Path Force Control System Bode Diagrams and Stability Margins ($G_p = 22.6$ dB and $P_p = 83.9^\circ$).

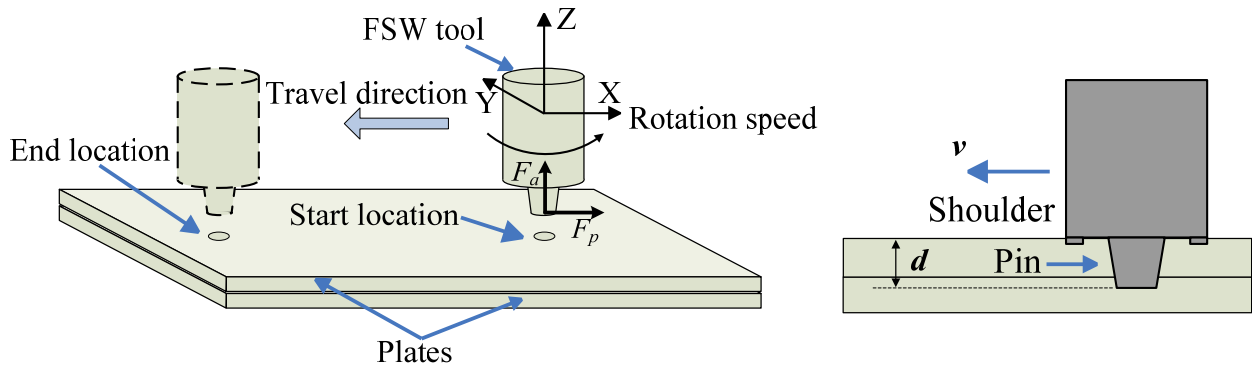


Figure 13: Lap Welding Experimental Setup.

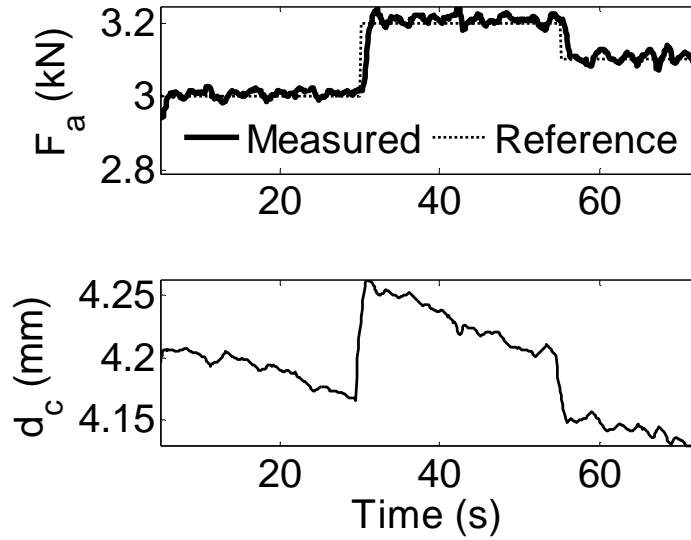


Figure 14: Experimental Results for Step Changes in Reference Axial Force ($v = 2.0 \text{ mm/s}$ and $\omega = 1600 \text{ rpm}$).

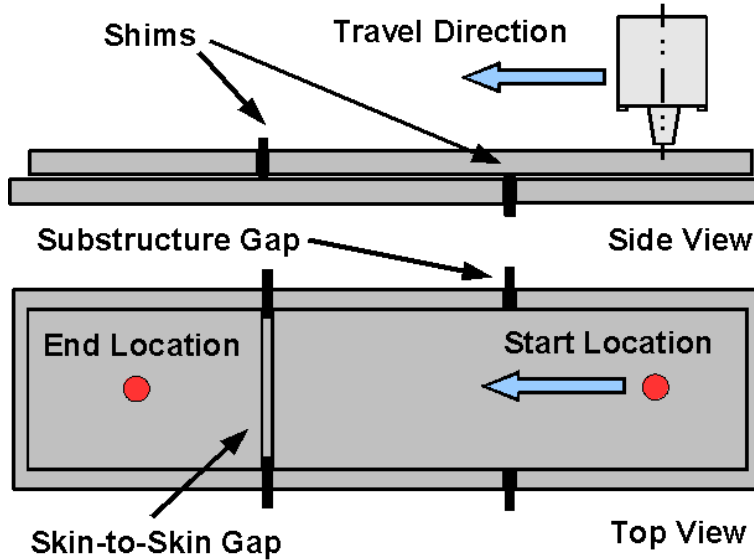


Figure 15: Four-Piece Lap Welding Experimental Setup with Substructure and Skin-to-Skin Gaps.

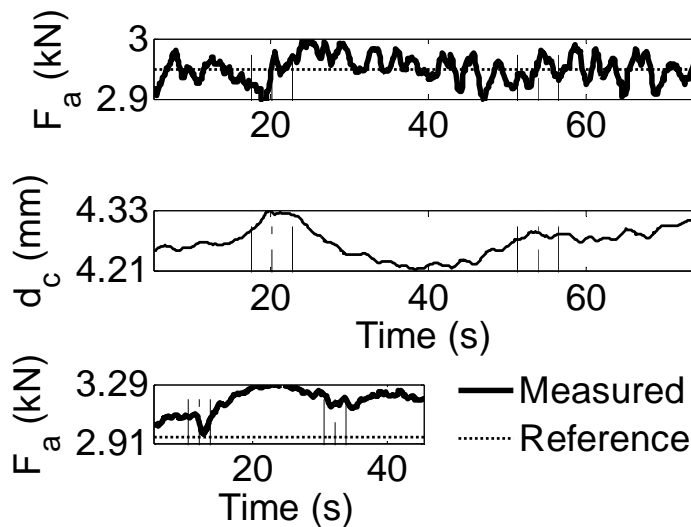


Figure 16: Four-Piece Experimental Results for Axial Force Control (test #4, top and middle subplots) and Constant Plunge Depth (test #10, bottom subplot, $d = 4.20 \text{ mm}$): $F_r = 2.95 \text{ kN}$, $v = 2.0 \text{ mm/s}$, $\omega = 2100 \text{ rpm}$, and $g = 0.381 \text{ mm}$.

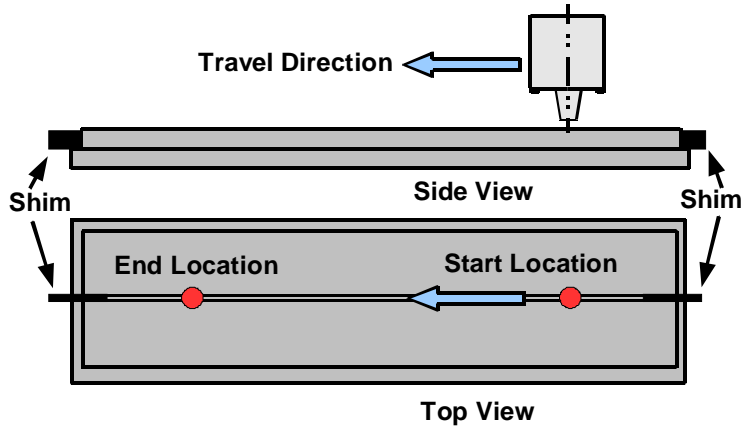


Figure 17: Experimental Setup for Welding Experiments along a Gap.

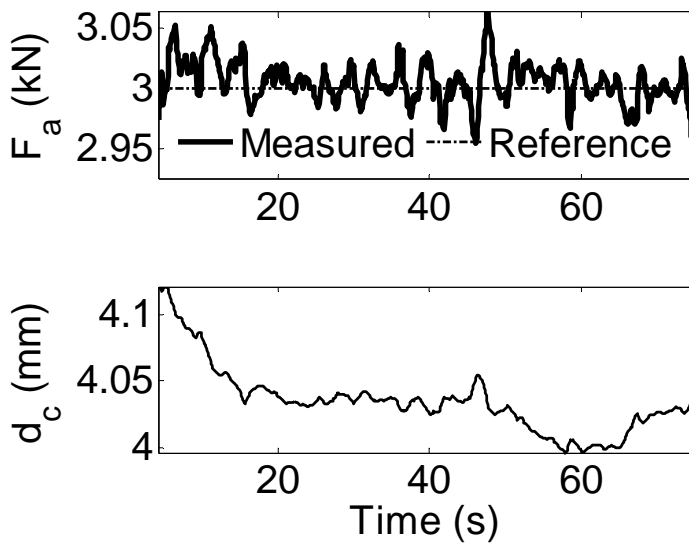


Figure 18: Axial Force and Plunge Depth when Welding along a Gap with Implementation of Axial Force Controller ($v = 2.0 \text{ mm/s}$, $\omega = 1600 \text{ rpm}$, $F_r = 3.00 \text{ kN}$, and tapered gap, $g = 0.381 \rightarrow 0.762 \text{ mm}$).

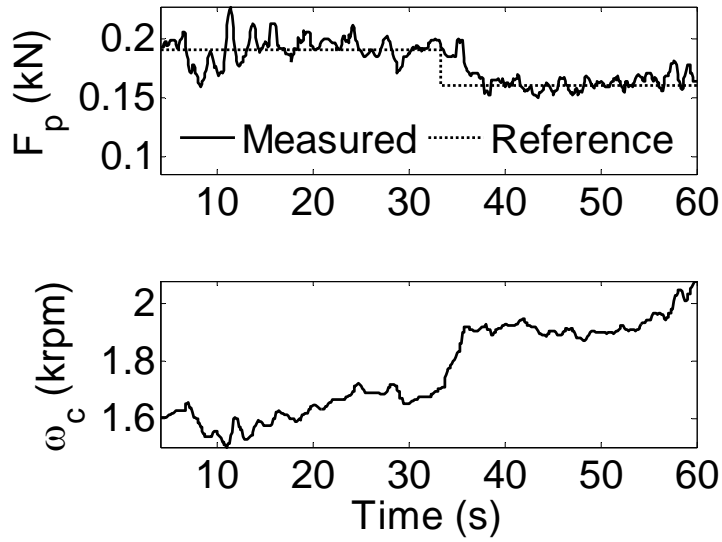


Figure 19: Path Force and Tool Rotation Speed for Path Force Controller ($d = 4.20 \text{ mm}$ and $v = 2.6 \text{ mm/s}$).

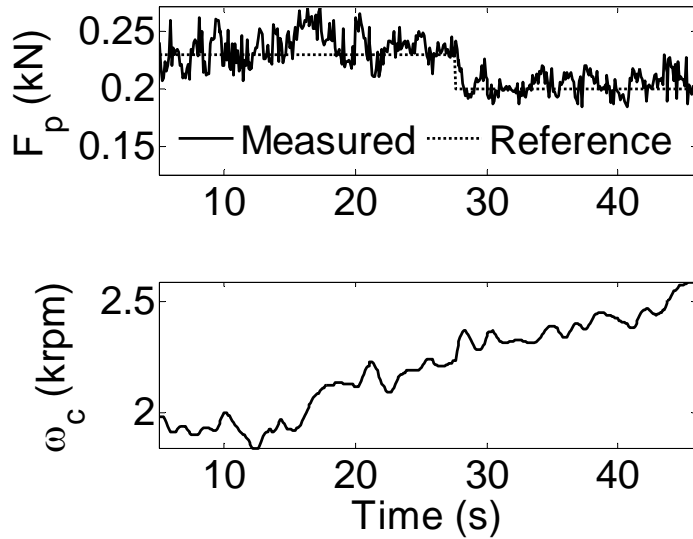


Figure 20: Path Force and Tool Rotation Speed when Welding along a Gap with Implementation of Path Force Controller ($d = 4.25 \text{ mm}$, $v = 3.2 \text{ mm/s}$, and tapered gap, $g = 0.381 \rightarrow 0.762 \text{ mm}$).

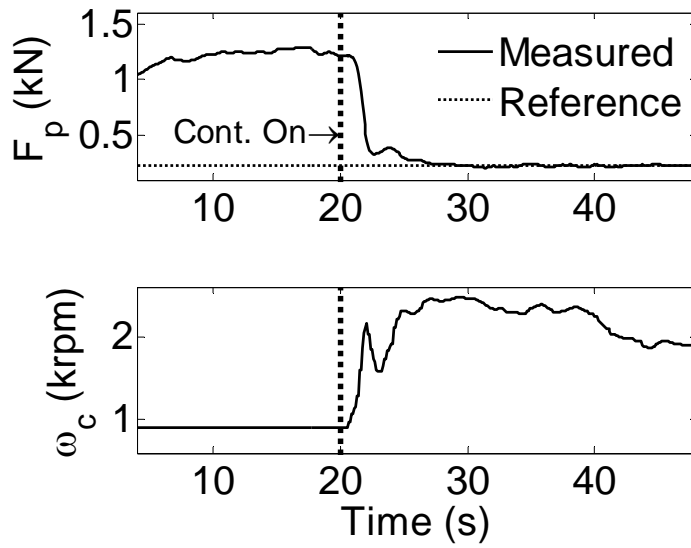


Figure 21: Path Force before and after Path Controller Implementation ($v = 3.2 \text{ mm/s}$, $d = 4.20 \text{ mm}$, and $F_r = 0.22 \text{ kN}$).

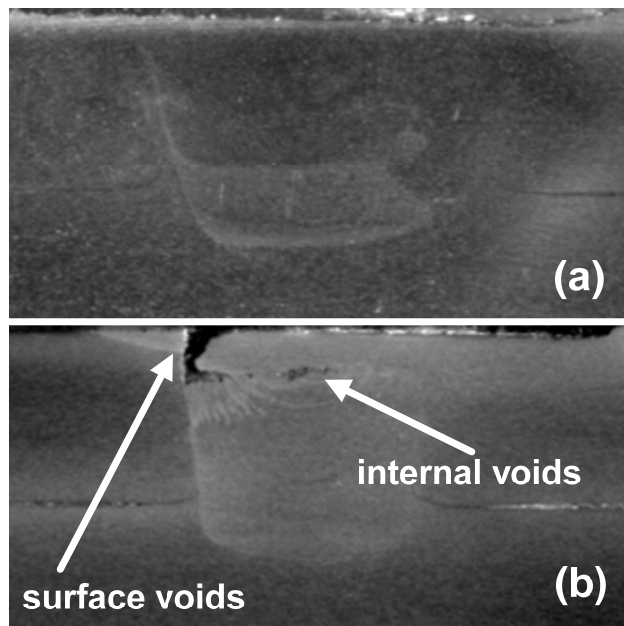


Figure 22: Nugget Cross Sections (a) with Path Force Control ($d = 4.20 \text{ mm}$, $v = 3.2 \text{ mm/s}$, and $F_r = 0.22 \text{ kN}$) and (b) without Path Force Control ($d = 4.20 \text{ mm}$, $v = 3.2 \text{ mm/s}$, and $\omega = 900 \text{ rpm}$).